

An improved method for the investigation of high-order harmonic generation from graphene

Zhong Guan(管仲), Lu Liu(刘璐), Guo-Li Wang(王国利), Song-Feng Zhao(赵松峰), Zhi-Hong Jiao(焦志宏), Xiao-Xin Zhou(周效信)

Citation: Chin. Phys. B . 2020, 29(10): 104206 . **doi:** 10.1088/1674-1056/abab76
Journal homepage: http://cpb.iphy.ac.cn; http://iopscience.iop.org/cpb

What follows is a list of articles you may be interested in

Role of Bloch oscillation in high-order harmonic generation from periodic structure

Lu Liu(刘璐), Jing Zhao(赵晶), Jian-Min Yuan(袁建民), Zeng-Xiu Zhao(赵增秀)

Chin. Phys. B . 2019, 28(11): 114205 . **doi:** 10.1088/1674-1056/ab47f7

Resolving multi-orbital effects on high harmonic generation from aligned N_2 molecules in linearly and elliptically polarized intense laser fields

Hong-Jing Liang(梁红静), Xin Fan(范鑫), Shuang Feng(冯爽), Li-Yu Shan(单立宇), Qing-Hua Gao(高庆华), Bo Yan(闫博), Ri Ma(马日), Hai-Feng Xu(徐海峰), Da-Jun Ding(丁大军)

Chin. Phys. B . 2019, 28(9): 094211 . **doi:** 10.1088/1674-1056/ab3440

Quantum interference of multi-orbital effects in high-harmonic spectra from aligned carbon dioxide and nitrous oxide

Hong-Jing Liang(梁红静), Xin Fan(范鑫), Shuang Feng(冯爽), Li-Yu Shan(单立宇), Qing-Hua Gao(高庆华), Bo Yan(闫博), Ri Ma(马日), Hai-Feng Xu(徐海峰)

Chin. Phys. B . 2019, 28(9): 094207 . **doi:** 10.1088/1674-1056/ab3438

Femtosecond enhancement cavity with kilowatt average power

Jin Zhang(张津), Lin-Qiang Hua(华林强), Shao-Gang Yu(余少刚), Zhong Chen(陈忠), Xiao-Jun Liu(柳晓军)

Chin. Phys. B . 2019, 28(4): 044206 . **doi:** 10.1088/1674-1056/28/4/044206

Effect of multiple rescattering processes on harmonic emission in spatially inhomogeneous field

Cai-Ping Zhang(张彩萍), Chang-Long Xia(夏昌龙), Xiang-Fu Jia(贾祥富), Xiang-Yang Miao(苗向阳)

Chin. Phys. B . 2018, 27(3): 034206 . **doi:** 10.1088/1674-1056/27/3/034206

An improved method for the investigation of high-order harmonic generation from graphene*

Zhong Guan(管仲)[1], Lu Liu(刘璐)[2], Guo-Li Wang(王国利)[1,†], Song-Feng Zhao(赵松峰)[1], Zhi-Hong Jiao(焦志宏)[1], and Xiao-Xin Zhou(周效信)[1,‡]

[1] College of Physics and Electronic Engineering, Northwest Normal University, Lanzhou 730070, China
[2] Department of Physics, College of Science, National University of Defense Technology, Changsha 410073, China

(Received 26 April 2020; revised manuscript received 15 June 2020; accepted manuscript online 1 August 2020)

High-order harmonic generation (HHG) of bulk crystals in strong laser field is typically investigated with semiconductor Bloch equations (SBEs). However, in the length gauge, it suffers from the divergence for the crystals with a zero band gap, such as graphene, using both Bloch- and Houston-states expansion methods. Here, we present a method of solving the SBEs based on time-dependent Bloch basis, which is equivalent to semiconductor Bloch equations in the velocity gauge. Using this method, we investigate the HHG of a single-layer graphene. It is found that our results for population are in good agreement with the other results. For a initial condition $p_y = 0$, we find the electrons just move in single valence band or conduction band, which are in accord with classical results. Our simulations on the HHG dependence of polarization of driving laser pulse confirm that 5th, 7th, and 9th harmonic yields increase to the maximal value when laser ellipticity $\varepsilon \approx 0.3$. What is more, similar to the case of atoms in the laser field, the total strength of 3rd harmonic decrease monotonically with the increase of ε. In addition, we simulate the dependence of HHG on crystallographic orientation with respect to the polarization direction of linear mid-infrared laser pulse, and the results reveal that for higher harmonics, their radiation along with the change of rotation angle θ reflects exactly the sixfold symmetry of graphene. Our method can be further used to investigate the behaviors of other materials having Dirac points (*i.e.*, surface states of topological insulators) in the strong laser fields.

Keywords: high-order harmonic generation, graphene, velocity gauge, divergence

PACS: 42.65.Ky, 42.50.Hz, 42.65.Re, 72.20.Ht **DOI:** 10.1088/1674-1056/abab76

1. Introduction

High-order harmonic generation (HHG) from atomic and molecular gases[1–4] has been a significant research topic in recent decades due to broad applications, such as diffractive imaging,[5] extracting of structural information of atoms or molecules,[6–12] probing magnetic dynamics.[13] More importantly, we can construct untrashort attosecond (as) pulses from harmonics,[14–19] which is an important tool for observing and controlling the ultrafast electronic dynamics in atoms and molecules. The physical picture of the atomic HHG process can be easily understood by the semiclassical three-step model.[20] According to this model, the cutoff energy of harmonic spectrum is $I_p + 3.17U_p$, where I_p is the atomic ionization potential, U_p is ponderomotive energy which is proportional to the intensity of laser pulse. Very recently, HHG from the crystalline solid[21–28] has also aroused great interests of researchers.[29–57] In this case, both experimental and theoretical investigations show that the harmonic cutoff energy of the first plateau increases linearly with the amplitude of field field. To interpret the mechanism of harmonic emission from crystals, a similar three-step model in momentum space is proposed on a basis of the energy band structure,[30] which can describe well the motion of electron-hole pairs in crystals: firstly, the electrons in the valence band driven by laser field tunnel to the conduction band, producing the electron-hole pairs; then, the electron-hole pairs oscillate in crystal lattice under laser filed and gain momentum (energy); finally, the electrons recombine with holes and radiate photons (HHG) later. Obviously, for crystal matters, the strength of HHG depends on the tunneling probability between valence band and conduction band, which is related to the energy gap and strength of laser, according to the Landau–Zaner law.

Theoretically, the semiconductor Bloch equations (SBEs) are often adopted to investigate the HHG emission from crystal, for it can easily introduce dephase time phenomenologically to take the relaxation effect into account.[35] However, for crystals with the zero band gap, such as graphene, when the initial electron momentum equals 0, the dipole moment will be divergent near the Dirac points in the length gauge. Thus, one must dig out the Dirac point or take a constant in the calculations,[58,59] which is inconvenient and might influence the accuracy of calculations. Alternatively, a simple transformation[60,61] is used to deal with the divergence due to

*Project supported by the National Natural Science Foundation of China (Grant Nos. 11764038, 11864037, 11765018, and 11664035) and the Science Foundation of Northwest Normal University, China (Grant No. NWNU-LKQN-17-1).

†Corresponding author. E-mail: wanggl@nwnu.edu.cn
‡Corresponding author. E-mail: zhouxx@nwnu.edu.cn

© 2020 Chinese Physical Society and IOP Publishing Ltd

the singular values of dipole moment near Dirac points. Furthermore, we could also solve directly time-dependent Dirac equation (TDDE).[62] However, in the last two cases it is difficult to consider the dephase time.

In this work, we present a method of solving SBEs in velocity gauge, which can avoid the divergence of dipole transition moment near Dirac points in a single-layer graphene. To confirm our method, we first compare our predictions for the population and electron current with other methods. Using our method, next we analyze the contributions of quantum trajectories around Dirac cone, and investigate the behavior of harmonic from graphene generated by elliptically polarized laser pulses. Finally we study HHG dependence on crystallographic orientation of graphene. The article is organized as follows. In Section 2, we give our theoretical framework. In Section 3, we show numerical simulations on HHG. Then we conclude our work in Section 4.

2. Theoretical method

Our theoretical approach is based on the time-dependent tight-binding (TB) approximation,[63–65] which has been extensively applied in the investigation of laser–graphene interaction.[58,59,66] For the graphene, the most important electronic states responsible for the harmonic emission are those arising from the carbon $2p_z$ orbitals, which form the extended π-bands. With the consideration of nearest-neighbor tight-binding of the π-electrons, we can easily obtain the energy bands. Near the Dirac points, energy bands calculated with T–B approximation are in accordance well with those obtained from first-principle calculations, *i.e.*, density functional theory, as long as the laser intensity is not too higher. The time-dependent Hamiltonian of graphene in the length gauge can be written as[67]

$$\hat{H}(t)=\begin{bmatrix}0 & \gamma f(\boldsymbol{k}(t))\\ \gamma f^{*}(\boldsymbol{k}(t)) & 0\end{bmatrix}, \tag{1}$$

where $\gamma=-3.03$ eV. The diagonalization of the matrix $\hat{H}(t)$ then yields energy eigenvalues, for the valence band $E_v(\boldsymbol{k}+\boldsymbol{A}(t))=-\gamma|f(\boldsymbol{k}+\boldsymbol{A}(t))|$ and the condution band $E_c(\boldsymbol{k}+\boldsymbol{A}(t))=\gamma|f(\boldsymbol{k}+\boldsymbol{A}(t))|$.[68] Considering the TB approximation, the matrix element $f(\boldsymbol{k}(t))$ can be written as

$$f(\boldsymbol{k}(t))=\sum_{\alpha=1}^{3}\mathrm{e}^{\mathrm{i}(\boldsymbol{k}+\boldsymbol{A}(t))\delta_\alpha} \tag{2}$$

with $\delta_1=(a/2)(1,\sqrt{3})$, $\delta_2=(a/2)(1,-\sqrt{3})$, $\delta_3=-a(1,0)$ are the locations of nearest neighbors separated by distance $a\approx 1.42$ Å. Considering the dephasing time,[36] the resulting dynamic equation in the length gauge reads[59,66]

$$\begin{aligned}\frac{\mathrm{d}}{\mathrm{d}t}\rho_{mn}=&-\mathrm{i}(E_m(\boldsymbol{k}+\boldsymbol{A}(t))-E_n(\boldsymbol{k}+\boldsymbol{A}(t)))\rho_{mn}\\&-\mathrm{i}\boldsymbol{F}(t)\{\boldsymbol{d}(\boldsymbol{k},t),\hat{\rho}\}_{mn}-\frac{\rho_{mn}}{T_2}.\end{aligned} \tag{3}$$

Here, ρ_{mn} is density matrix comprised of the inter-band polarization $(m\neq n)$ and the population probability in a band $(m=n)$, $\boldsymbol{F}(t)$ is the laser field, and T_2 is dephase time.[58] $\boldsymbol{d}(\boldsymbol{k},t)$ denotes the dipole moment

$$\boldsymbol{d}_{mn}(\boldsymbol{k}+\boldsymbol{A}(t))=\mathrm{i}\{[\langle u_m(t)|\bigtriangledown_{\boldsymbol{k}}|u_n(t)\rangle]\}, \tag{4}$$

where $u_{m,n}$ is energy eigenvectors with the Houston basis. Then we could obtain an explicit expression for $\boldsymbol{d}_{cv}(\boldsymbol{k})$ as

$$\boldsymbol{d}_{cv}(\boldsymbol{k})=\frac{a}{2|f(\boldsymbol{k})|^2}\left\{\left[\frac{1}{\sqrt{3}}\cos\left(\frac{\sqrt{3}}{2}ak_x\right)\cos\left(\frac{1}{2}ak_y\right)-\frac{1}{\sqrt{3}}\cos(ak_y)\right]\hat{x}+\left[\sin\left(\frac{\sqrt{3}}{2}ak_x\right)\sin\left(\frac{1}{2}ak_y\right)\right]\hat{y}\right\}. \tag{5}$$

Obviously, $\boldsymbol{d}_{cv}(\boldsymbol{k})$ will diverge near Dirac points due to its vanishing band gap. This defect also exists in the case of Bloch basis in the length gauge.[69]

In order to avoid this divergence, we can calculate current in velocity gauge with Bloch basis. We can write $\hat{H}(t)$ as

$$\hat{H}(t)=\hat{H}_0+\boldsymbol{A}(t)\cdot\boldsymbol{P}+\boldsymbol{A}(t)^2=\sum_{\alpha=1}^{3}\hat{H}_0^{\alpha}+\sum_{\alpha=1}^{3}\hat{H}_{\mathrm{I}}^{\alpha}, \tag{6}$$

where $\boldsymbol{P}$ is the momentum operator, and

$$\begin{aligned}\hat{H}_0=&\gamma\begin{bmatrix}0 & \mathrm{e}^{\mathrm{i}\boldsymbol{k}\delta_1}\\ \mathrm{e}^{-\mathrm{i}\boldsymbol{k}\delta_1} & 0\end{bmatrix}+\gamma\begin{bmatrix}0 & \mathrm{e}^{\mathrm{i}\boldsymbol{k}\delta_2}\\ \mathrm{e}^{-\mathrm{i}\boldsymbol{k}\delta_2} & 0\end{bmatrix}\\&+\gamma\begin{bmatrix}0 & \mathrm{e}^{\mathrm{i}\boldsymbol{k}\delta_3}\\ \mathrm{e}^{-\mathrm{i}\boldsymbol{k}\delta_3} & 0\end{bmatrix},\end{aligned} \tag{7}$$

$$\hat{H}_I^{\alpha}(t)=\gamma\begin{bmatrix}0 & \mathrm{e}^{\mathrm{i}\boldsymbol{k}\delta_\alpha}\\ \mathrm{e}^{-\mathrm{i}\boldsymbol{k}\delta_\alpha} & 0\end{bmatrix}$$

$$\times\begin{bmatrix}\mathrm{e}^{-\mathrm{i}\boldsymbol{A}(t)\delta_\alpha}-1 & 0\\ 0 & \mathrm{e}^{\mathrm{i}\boldsymbol{A}(t)\delta_\alpha}-1\end{bmatrix}. \tag{8}$$

Utilizing Bloch basis as unitary transformation matrix

$$U=\frac{1}{\sqrt{2}}\begin{bmatrix}\mathrm{e}^{\mathrm{i}\theta_{f(\boldsymbol{k})}} & -\mathrm{e}^{\mathrm{i}\theta_{f(\boldsymbol{k})}}\\ 1 & 1\end{bmatrix}, \tag{9}$$

$\theta_{f(\boldsymbol{k})}$ is the phase angle, *i.e.*,

$$\tan(\theta_{f(\boldsymbol{k})})=\frac{\mathrm{Im}(f(\boldsymbol{k}))}{\mathrm{Re}(f(\boldsymbol{k}))},$$

we have

$$\begin{aligned}U\hat{H}_0^{\alpha}U^{\dagger}&=U\begin{bmatrix}0 & \gamma\mathrm{e}^{\mathrm{i}\boldsymbol{k}\delta_\alpha}\\ \gamma\mathrm{e}^{-\mathrm{i}\boldsymbol{k}\delta_\alpha} & 0\end{bmatrix}U^{\dagger},\\ U\hat{H}_I^{\alpha}U^{\dagger}&=U\begin{bmatrix}0 & \gamma\mathrm{e}^{\mathrm{i}\boldsymbol{k}\delta_\alpha}\\ \gamma\mathrm{e}^{-\mathrm{i}\boldsymbol{k}\delta_\alpha} & 0\end{bmatrix}U^{\dagger}\end{aligned} \tag{10}$$

$$\times U\begin{bmatrix} \mathrm{e}^{-\mathrm{i}\boldsymbol{A}(t)\delta_\alpha}-1 & 0 \\ 0 & \mathrm{e}^{\mathrm{i}\boldsymbol{A}(t)\delta_\alpha}-1 \end{bmatrix}U^\dagger. \quad (11)$$

Thus we obtain the time-dependent Hamiltonian in the Bloch basis

$$\hat{H}_B(t)=U\hat{H}(t)U^\dagger=\gamma\begin{bmatrix} W_1(t) & W_2(t) \\ W_3(t) & W_4(t) \end{bmatrix} \quad (12)$$

with

$$W_1(t)=-f(\boldsymbol{k}(t))\,\mathrm{e}^{-\mathrm{i}\theta_{f(\boldsymbol{k})}}-f^*(\boldsymbol{k}(t))\,\mathrm{e}^{\mathrm{i}\theta_{f(\boldsymbol{k})}}, \quad (13)$$
$$W_2(t)=-f(\boldsymbol{k}(t))\,\mathrm{e}^{-\mathrm{i}\theta_{f(\boldsymbol{k})}}+f^*(\boldsymbol{k}(t))\,\mathrm{e}^{\mathrm{i}\theta_{f(\boldsymbol{k})}}, \quad (14)$$
$$W_3(t)=f(\boldsymbol{k}(t))\,\mathrm{e}^{-\mathrm{i}\theta_{f(\boldsymbol{k})}}-f^*(\boldsymbol{k}(t))\,\mathrm{e}^{\mathrm{i}\theta_{f(\boldsymbol{k})}}, \quad (15)$$
$$W_4(t)=f(\boldsymbol{k}(t))\,\mathrm{e}^{-\mathrm{i}\theta_{f(\boldsymbol{k})}}+f^*(\boldsymbol{k}(t))\,\mathrm{e}^{\mathrm{i}\theta_{f(\boldsymbol{k})}}, \quad (16)$$

and 2-band equations

$$\frac{\mathrm{d}}{\mathrm{d}t}C_\mathrm{v}=\frac{\gamma}{2}\mathrm{i}[-W_1(t)C_\mathrm{v}-W_2(t)C_\mathrm{c}], \quad (17)$$
$$\frac{\mathrm{d}}{\mathrm{d}t}C_\mathrm{c}=\frac{\gamma}{2}\mathrm{i}[-W_3(t)C_\mathrm{v}-W_4(t)C_\mathrm{c}], \quad (18)$$

where C_v and C_c are probability amplitudes in valence band and conduction band, respectively. Thus, $C_\mathrm{v}C_\mathrm{v}^\dagger$ is valence population, and $C_\mathrm{c}C_\mathrm{c}^\dagger$ is conduction population.

Next following the Ref. [55], we obtain following dynamic equations

$$\frac{\mathrm{d}}{\mathrm{d}t}\rho(\boldsymbol{k},t)=-\mathrm{i}A_4^*\rho(\boldsymbol{k},t)+\mathrm{i}A_1^*\rho(\boldsymbol{k},t) -\mathrm{i}A_3(1-f_\mathrm{e}-f_\mathrm{h})-\gamma_\mathrm{r}\rho(\boldsymbol{k},t), \quad (19)$$
$$\frac{\mathrm{d}}{\mathrm{d}t}f_\mathrm{e}=2\mathrm{Im}\,[A_3^*\rho(\boldsymbol{k},t)]-\gamma_\mathrm{l}f_\mathrm{e}, \quad (20)$$
$$\frac{\mathrm{d}}{\mathrm{d}t}f_\mathrm{h}=2\mathrm{Im}\,[-A_2^*\rho(\boldsymbol{k},t)]-\gamma_\mathrm{l}f_\mathrm{h}, \quad (21)$$

where $\rho(\boldsymbol{k},t)$ is the inter-band polarization, f_e and f_h denote electron and hole population, respectively, and

$$A_1(t)=-\frac{\gamma}{2}[f(\boldsymbol{k}(t))\,\mathrm{e}^{-\mathrm{i}\theta_{f(\boldsymbol{k})}}+f^*(\boldsymbol{k}(t))\,\mathrm{e}^{\mathrm{i}\theta_{f(\boldsymbol{k})}}], \quad (22)$$
$$A_2(t)=-\frac{\gamma}{2}[f(\boldsymbol{k}(t))\,\mathrm{e}^{-\mathrm{i}\theta_{f(\boldsymbol{k})}}-f^*(\boldsymbol{k}(t))\,\mathrm{e}^{\mathrm{i}\theta_{f(\boldsymbol{k})}}], \quad (23)$$
$$A_3(t)=\frac{\gamma}{2}[f(\boldsymbol{k}(t))\,\mathrm{e}^{-\mathrm{i}\theta_{f(\boldsymbol{k})}}-f^*(\boldsymbol{k}(t))\,\mathrm{e}^{\mathrm{i}\theta_{f(\boldsymbol{k})}}], \quad (24)$$
$$A_4(t)=\frac{\gamma}{2}[f(\boldsymbol{k}(t))\,\mathrm{e}^{-\mathrm{i}\theta_{f(\boldsymbol{k})}}+f^*(\boldsymbol{k}(t))\,\mathrm{e}^{\mathrm{i}\theta_{f(\boldsymbol{k})}}]. \quad (25)$$

Here, γ_r and γ_l are the transverse and longitudinal relaxation constants, respectively.[36] In our calculations, $\gamma_\mathrm{r}=0.2\omega$, $\gamma_\mathrm{r}=0.05\omega$. In the most simplified case, $\gamma|f(\boldsymbol{k})|\approx(k^2/2m_\mathrm{u}+E_\mathrm{g}/2)$ and $\theta_{f(\boldsymbol{k})}=\theta_{\boldsymbol{k}}$. As shown in Fig. 1 for the first Brillouin zone (BZ) of graphene, we can find two inequivalent Dirac points referred to as K and K', which are degenerate in terms of energy. We can get two equation sets for them. Around K we have

$$\frac{\mathrm{d}}{\mathrm{d}t}\rho_{\boldsymbol{k}}=-\mathrm{i}B_4\rho_{\boldsymbol{k}}+\mathrm{i}B_1\rho_{\boldsymbol{k}}-\mathrm{i}B_3(1-f_\mathrm{e}-f_\mathrm{h})-\gamma_\mathrm{r}\rho_{\boldsymbol{k}}, \quad (26)$$

$$\frac{\mathrm{d}}{\mathrm{d}t}f_\mathrm{e}=2\mathrm{i}\mathrm{Im}(B_3^*\rho_{\boldsymbol{k}})-\gamma_\mathrm{l}f_\mathrm{e}, \quad (27)$$
$$\frac{\mathrm{d}}{\mathrm{d}t}f_\mathrm{h}=-2\mathrm{i}\mathrm{Im}(B_2^*\rho_{\boldsymbol{k}})-\gamma_\mathrm{l}f_\mathrm{h}, \quad (28)$$

with

$$B_1(t)=E_v(\boldsymbol{k})-v_\mathrm{f}\cos(\theta_{\boldsymbol{k}})A_x-v_\mathrm{f}\sin(\theta_{\boldsymbol{k}})A_y, \quad (29)$$
$$B_2(t)=-\mathrm{i}v_\mathrm{f}\sin(\theta_{\boldsymbol{k}})A_x+\mathrm{i}v_\mathrm{f}A_y\cos(\theta_{\boldsymbol{k}}), \quad (30)$$
$$B_3(t)=\mathrm{i}v_\mathrm{f}\sin(\theta_{\boldsymbol{k}})A_x-\mathrm{i}v_\mathrm{f}A_y\cos(\theta_{\boldsymbol{k}}), \quad (31)$$
$$B_4(t)=E_\mathrm{c}(\boldsymbol{k})+v_\mathrm{f}\cos(\theta_{\boldsymbol{k}})A_x+v_\mathrm{f}\sin(\theta_{\boldsymbol{k}})A_y, \quad (32)$$

here v_f is Fermi velocity, $v_\mathrm{f}\approx c/300$, c is velocity of light. For point K' we have similar equations as for K, instead of substituting B_2 with $-B_2$ and B_3 with $-B_3$.

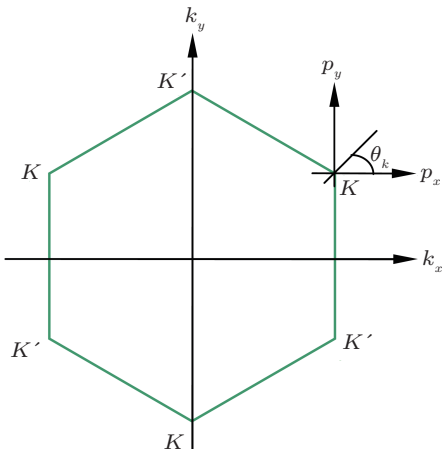


Fig. 1. The first Brillouin zone in graphene.

The above equation sets can be numerically solved for each independent $\boldsymbol{k}$ by the classical fourth-order Runge–Kutta method combining with an adaptive step-size routine. We then obtain the single-electron current. Around K, we have

$$j_x^K(t)=(1-f_\mathrm{e}-f_\mathrm{h})\cos(\theta_{\boldsymbol{k}})-2\mathrm{Im}(\rho_{\boldsymbol{k}})\sin(\theta_{\boldsymbol{k}}), \quad (33)$$
$$j_y^K(t)=(1-f_\mathrm{e}-f_\mathrm{h})\sin(\theta_{\boldsymbol{k}})+2\mathrm{Im}(\rho_{\boldsymbol{k}})\cos(\theta_{\boldsymbol{k}}). \quad (34)$$

Around K', we have

$$j_x^{K'}(t)=(1-f_\mathrm{e}-f_\mathrm{h})\cos(\theta_{\boldsymbol{k}})+2\mathrm{Im}(\rho_{\boldsymbol{k}})\sin(\theta_{\boldsymbol{k}}), \quad (35)$$
$$j_y^{K'}(t)=(1-f_\mathrm{e}-f_\mathrm{h})\sin(\theta_{\boldsymbol{k}})-2\mathrm{Im}(\rho_{\boldsymbol{k}})\cos(\theta_{\boldsymbol{k}}). \quad (36)$$

After we taking into account the Fermi distribution and initial condition $1-f_\mathrm{e}-f_\mathrm{h}=-F(\boldsymbol{p})+F(-\boldsymbol{p})$, where $F(\boldsymbol{p})=1+\exp[(E_n(\boldsymbol{p})-u)/k_\mathrm{B}T]^{-1}$, with u, k_B, and T being the chemical potential, Boltzman constant, and temperature, respectively, we obtain the total integrated electric current $\boldsymbol{J}(t)$. The Harmonic spectrum is given by $I(\omega)\propto|\omega\boldsymbol{J}(\omega)|^2$, $\boldsymbol{J}(\omega)$ is Fourier transform of the $\boldsymbol{J}(t)$.

If we want to further gain the information from valence and conduction bands, at each time, we can easily get density-matrix elements ρ_{mn} by simple unitary transformation

$$\rho_{cc}=0.25(Z_3^*Z_3)(1-f_\mathrm{e})+0.25(Z_3^*Z_4)\rho_{\boldsymbol{k}}$$

$$+0.25(Z_4^*Z_3)\rho_{\boldsymbol{k}}^*+0.25(Z_4^*Z_4)f_{\rm h}, \tag{37}$$

$$\rho_{cv}=0.25(Z_3^*Z_1)(1-f_{\rm e})+0.25(Z_3^*Z_2)\rho_{\boldsymbol{k}}$$
$$+0.25(Z_4^*Z_1)\rho_{\boldsymbol{k}}^*+0.25(Z_4^*Z_2)f_{\rm h}, \tag{38}$$

$$\rho_{vv}=0.25(Z_1^*Z_1)(1-f_{\rm e})+0.25(Z_1^*Z_2)\rho_{\boldsymbol{k}}$$
$$+0.25(Z_2^*Z_1)\rho_{\boldsymbol{k}}^*+0.25(Z_2^*Z_2)f_{\rm h}, \tag{39}$$

where

$$Z_1(t)=(\mathrm{e}^{-\mathrm{i}\theta_{f(\boldsymbol{k}(t))}}\mathrm{e}^{-\mathrm{i}\theta_{f(\boldsymbol{k})}}+1)/2, \tag{40}$$

$$Z_2(t)=(-\mathrm{e}^{-\mathrm{i}\theta_{f(\boldsymbol{k}(t))}}\mathrm{e}^{-\mathrm{i}\theta_{f(\boldsymbol{k})}}+1)/2, \tag{41}$$

$$Z_3(t)=Z_2(t), \tag{42}$$

$$Z_4(t)=Z_1(t). \tag{43}$$

From the above equations, we see that there are no divergence around Dirac points in our method.

3. Results and discussion

3.1. Confirmation of our method

3.1.1. Comparison of population for conduction band between velocity gauge and two-band model

In the following, we aim to confirm the validity of our method. We first compare our calculated conduction band population with those from Ref. [58], in which Kelardeh *et al*. investigated the charge transfer process in graphene by a two-band model based on Houston basis. The laser pulse has the form of

$$F(t)=F_0\,\mathrm{e}^{-u^2}(1-2u^2), \tag{44}$$

where F_0 is the amplitude of laser pulse, $u=t/\tau$, $\tau=1$ fs, laser frequency $\omega\approx 0.057$ a.u. We compare $\rho_{cc}(\boldsymbol{k},t)$ at the end of laser pulse for two different laser amplitudes in Fig. 2.

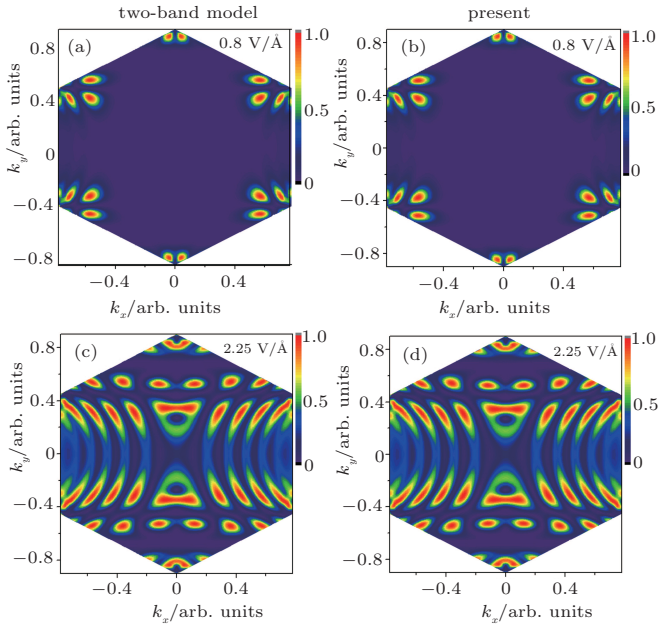


Fig. 2. Comparison of our calculated conduction band population $\rho_{cc}(\boldsymbol{k},t)$ in the velocity gauge (right column) with those from the two-band model (left column) given in Ref. [58] for panels (a) and (b) $F_0=0.8$ V/Å and panels (c) and (d) $F_0=2.25$ V/Å.

One can see that the electrons movement under laser field lead to interference fringes, and at the end of pulse, the distribution becomes completely symmetric which can be modulated by laser amplitude. Our results with SBEs in the velocity gauge agree very well with those from the two-band model, for both amplitudes, *i.e*., $F_0=0.8$ V/Å and a higher one of 2.25 V/Å.

In Fig. 3, we further compare $\rho_{cc}(\boldsymbol{k},t)$ obtained with two methods for $t=0.75$ fs and $t=2.25$ fs. It shows again that our results are in good accordance with those from two-band model.[58]

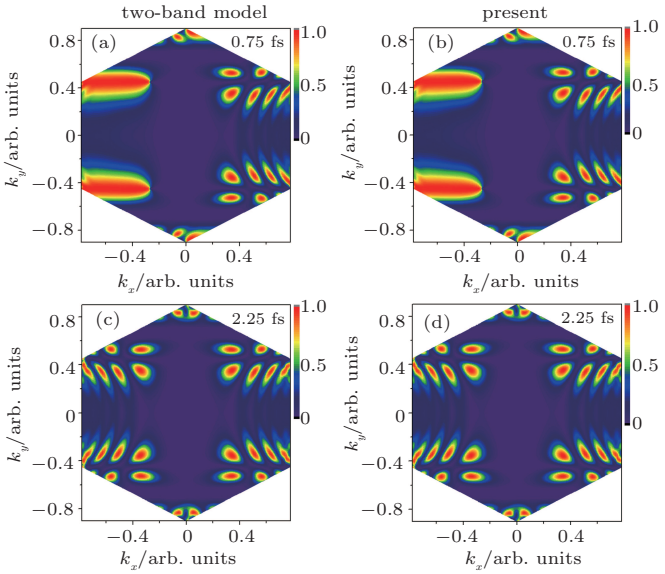


Fig. 3. The same as Fig. 2, but for panels (a) and (b) $t=0.75$ fs and panels (c) and (d) $t=2.25$ fs with the same $F_0=1.0$ V/Å.

3.1.2. Comparison of single-electron current calculated from SBE and TDDE

Next, we compare current calculated by our method (Eqs. (33)–(36)) with those from solving time-dependent Dirac equation (TDDE).[62] The laser field used in the simulation is a flat-top pulse with a half-cycle ramp on

$$\boldsymbol{A}(t)=\begin{cases}0, & \text{if } (t<0),\\ A_0\dfrac{\omega t}{\pi}\sin(\omega t), & \text{if } (0\le t<\pi/\omega),\\ A_0\sin(\omega t), & \text{if } (\pi/\omega\le t),\end{cases} \tag{45}$$

where $A_0>|p_x|$, the field strength is 27.5 kV/cm, carrier frequency is 1 THz. In Fig. 4 we show the normalized single-electron current calculated by two methods for three different p_y values. Obviously, our results agree well with those from TDDE in all cases.

We note that another advantage of our method is that in our simulations without solving the gradient of $\boldsymbol{d}_{cv}(\boldsymbol{k})$,[55] which promotes calculation efficiency greatly. In addition, if we use the Houston basis, it is difficult to obtain correct current

near Dirac points, although it provides an advantage of decoupling the states at different crystal momentum. From Fig. 4(a) we see that a step transition occurred in the j_x calculated with the Houston basis, which is unphysical.

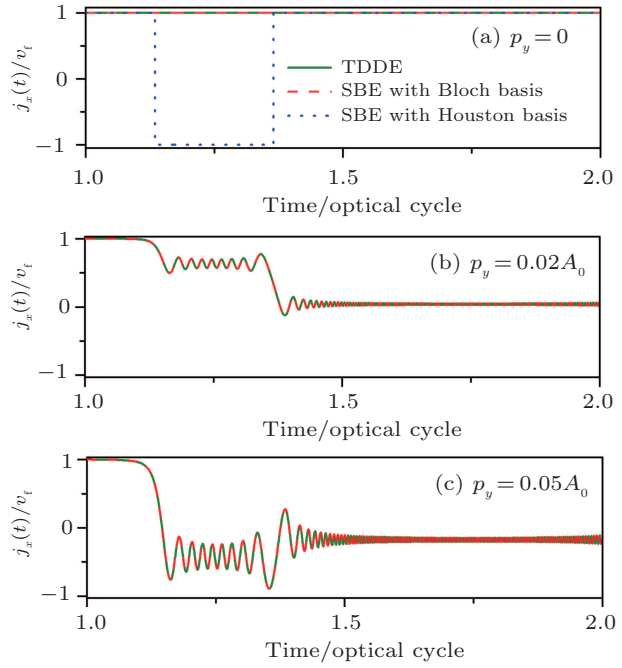


Fig. 4. Comparison of the temporal evolution of the normalized single-electron current calculated by our method and those from TDDE for (a) $p_y = 0$, (b) $p_y = 0.02A_0$, and (c) $p_y = 0.05A_0$. In all the cases $p_x/eA_0 = -0.75$. In Fig. 4(a) we also show the result with Houston basis.

3.2. Application of our method

3.2.1. The contributions from quantum trajectories

After proving our method is feasible and effective, we show a few examples of its applications in simulation of HHG from graphene. Firstly, we strive to extract the contributions of individual quantum trajectories around single Dirac cone, which is important in analyzing electron dynamic motion. To achieve this we use the windowed Fourier transform (WFT), form of the wave function is given in Ref. [70]. In that paper, Chizhova *et al*. showed that the individual quantum trajectories can be extracted by solving TDDE.

In Fig. 5, we show the laser vector potential and generated electron current, wave packets for three initial energies. For initial energy of $|E_n| < v_f A_0$ and zero p_y, one can see that electron moves in valence band or conduction band driven by laser pulse with a constant current [Figs. 5(a) and 5(b)], the response features intraband dynamics.

Considering an electron with initial momentum p_x=0.8A_0, p_y=0.1A_0, it moves initially in the valence band. When laser field reaches its maximum after one optical cycle, electron is driven up to the Dirac point, then the electronic wave packet splits into two parts, one is excited to the conduction band via inter-band Landau-Zener tunneling, while the other remains in the valence band [see Fig. 5(d)]. The superposition of two wave packets results in high-frequency oscillations of the current j_x [Fig. 5(c)], which is determined by coherent superposition of inter-band and intra-band dynamics. The strength of Landau–Zener tunneling rate depends exponentially on the energy gap between the two cones at the p_y = constant conical intersection. The highest oscillation frequency is realized when the two paths reach their maximal separation in energy (near 1.5T).

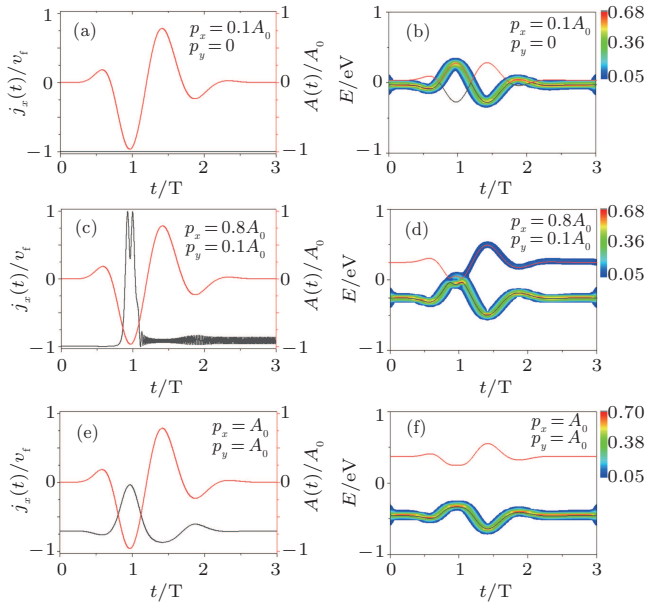


Fig. 5. Left column: the vector potential of laser pulse and electron current; Right column: the time evolution of the wave packet (red and black lines are classical trajectories).

When initial energies $|E_n| \approx v_f A_0$ and $p_y \approx A_0$, the total current just shows intra-band dynamics, and electrons move in valence band under laser pulses due to a big energy gap.

3.2.2. Harmonic dependence on ellipticity of driving laser pulse

Unlike atom and uniaxial hexagonal crystal, HHG from graphene shows abnormal dependence of harmonic strength on the polarization of driving laser field.[71] Now we move to this issue. We simulate harmonic spectra with the following laser pulse:

$$\boldsymbol{F}(t) = \frac{F_0}{\sqrt{1+\varepsilon^2}} f(t)[\cos(\omega t)\hat{e}_x - \varepsilon \sin(\omega t)\hat{e}_y] \tag{46}$$

with laser pulse shape of $f(t) = \cos^2(\pi t/nT)$, $n = 8$, the central wavelength of 3200 nm, and the laser field strength of $F_0 = 4.38 \times 10^6$ V/cm. In our calculations, we artificially limit the Brillouin zone $|\boldsymbol{k} - \boldsymbol{k}_D| < 0.2$ according to Ref. [59]. Figure 6 exhibits our simulated results for three laser ellipticities, *i.e*., for $\varepsilon = 0$, 0.3, and 1.0. From the figure, we see that for the circularly polarized pulse, the harmonic radiation is efficiently switched off. However, the HHG yields generated in

linear laser pulse is weaker than those in an elliptically polarized laser field, except for the 3rd harmonics.

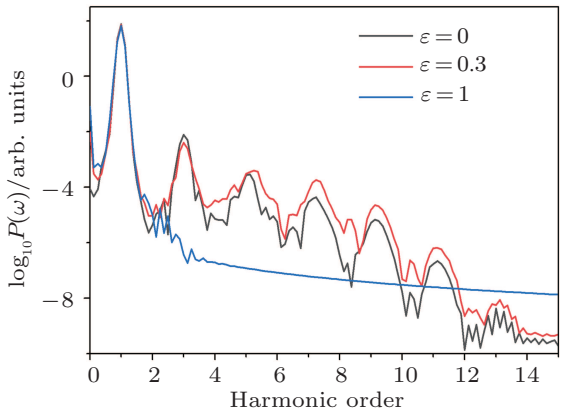


Fig. 6. Comparison of harmonic spectra of graphene generated by laser fields with different ellipticity.

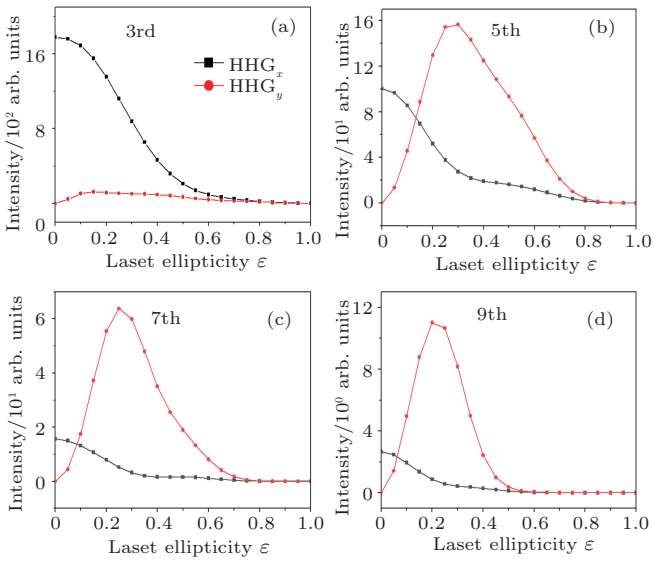


Fig. 7. The dependence of intensity in two perpendicular directions (x and y) of harmonics 3rd, 5th, 7th, and 9th on the ellipticity of driving laser pulse.

In Fig. 7, we show more detailed dependence of intensity of harmonics 3rd, 5th, 7th, and 9th on the ellipticity of driving laser pulse. It is found that this dependence strongly relies on the harmonic radiated direction. In the y direction, the 3rd harmonic emission has a weak dependence on ε and reaches maximal value at $\varepsilon \approx 0.15$, while strong radiation in the x direction, and the total harmonic yields decrease monotonically with the increasing of parameter ε. This trend is similar to the case of harmonic radiated from atoms.[72] For the 5th, 7th, and 9th harmonics, their strength in two directions intersect at one laser ellipticity, and the x-direction harmonic intensity decays quickly with the change of parameter ε, while the y-direction harmonics increases to a maximal value at a certain ε (for example, $\varepsilon \approx 0.3$ for the 5th, 7th harmonics, $\varepsilon \approx 0.2$ for the 9th harmonics) and then decreases monotonically with further increasing of ε. It is worth mentioning that the total harmonic yields will display a non-monotonic variation, which can well match the recent experimental observation[71] and theoretical simulations.[59]

3.2.3. Effect of crystal orientation on HHG

The polarization direction of laser pulse with respect to the crystal axis is another factor that influence the harmonic emission.[73] However, the orientation dependence of the 7th harmonic does not reflect the hexagonal structure of graphene in an experimental study.[71] Here we reinvestigate this issue using our method. We simulate harmonic spectra with a linear laser field as described by Eq. (46) with $F_0 = 8.7 \times 10^6$ V/cm, $\varepsilon = 0$, and the laser duration is 12 optical cycles. Figure 8 shows our main results.

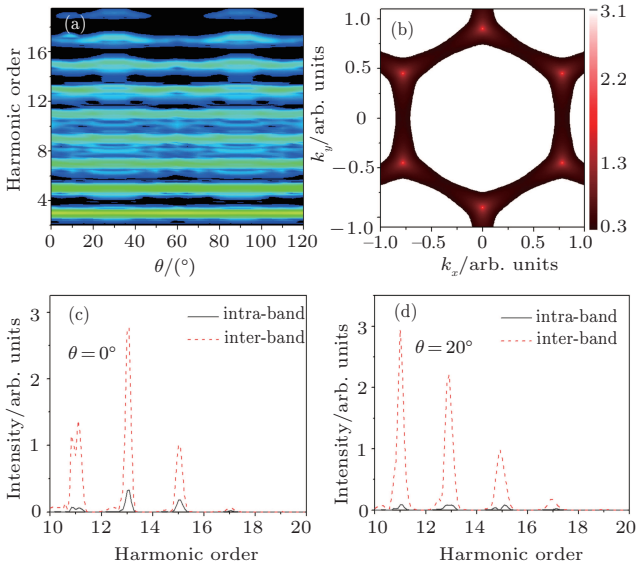


Fig. 8. (a) Harmonic radiation with different rotation angle θ. (b) The inter-band polarization $\boldsymbol{d}_{cv}(\boldsymbol{k})$ as a function of the crystal momentum k. (c) and (d) Harmonic spectra generated from inter-band polarization and intra-band current for θ of 0° and 20°, respectively.

From Fig. 8(a), we can see that for lower harmonics, same as experimental findings,[71] their strength almost has no dependence on the laser rotation angle, while for the higher harmonics, their intensities change periodically twice with the increasing the θ from 0° to 120°, which indicates sixfold symmetry structure of graphene.

These results can be understood as follows. Under a weaker laser field, electrons moves mainly around Dirac cones, and these electrons will contribute to lower order harmonics, so band structure of a solid appears unimportant. With the increase of field strength, electrons are driven beyond Dirac cones, inter-band current will play major role and give rise to higher harmonics [Figs. 8(c) and 8(d)], and results reveal a strong link between sixfold symmetry structure of graphene and inter-band polarization [Fig. 8(b)].

4. Conclusion

In summary, in order to simulate the HHG from graphene we propose a new efficient theoretical approach in this paper. Unlike the previous methods, we solve the semiconductor Bloch equations in velocity gauge, which has the advantages of no defect of divergence of dipole transition moment around Dirac points, avoiding the solve the gradient of dipole transition moment.

Using our method, we have investigated some typical issues associated with HHG from graphene. Our simulations demonstrate that our method can be used successfully to analyze the electron dynamics in valence band and conduction band, especially for the initial condition $p_y = 0$. We show that harmonic yields in two perpendicular directions depend differently on the ellipticity of driving laser pulse, and the 3rd-harmonic intensity decreases monotonically with the laser ellipticity, while the 5th, 7th, and 9th harmonics can be enhanced at a particular ellipticity, and it reaches to its maximum when $\varepsilon \approx 0.3$, which are in agreement with the experimental findings. Our simulations for the HHG dependence on the crystal orientation also show that sixfold symmetry of graphene can be retrieved from higher harmonics, which can be further confirmed in the experiments.

In addition to graphene, our method can be also used to investigate the interaction of strong laser fields with other zero-band-gap systems, such as surface states of topological insulators.[74,75]

References

[1] Xia C L, Lan Y Y, Li Q Q and Miao X Y 2019 *Chin. Phys. B* **28** 103203
[2] Zhang H D, Guo J, Shi Y, Du H, Liu H F, Huang X R, Liu X S and Jing Jun 2017 *Chin. Phys. Lett.* **34** 014206
[3] Pan Y, Guo F M, Yang Y J and Ding D J 2019 *Chin. Phys. B* **28** 113201
[4] Guo C X, Jiao Z H, Zhou X X and Li P C 2020 *Acta Phys. Sin.* **69** 074203 (in Chinese)
[5] Popmintchev T, Chen M C, Popmintchev D, Arpin P, Brown S, Ališauskas S, Andriukaitis G, Balčiunas T, Mücke Q D, Pugzlys A, Baltuška A, Shim B, Schrauth S E, Gaeta A, Hernández-García C, Plaga L, Becker A, Jaron-Becker A, Murnane M M and Kapteyn H C 2012 *Science* **336** 1287
[6] He L X, Lan P F, Le A T, Wang B N, Wang B C, Zhu X S, Lu P X and Lin C D 2018 *Phys. Rev. Lett.* **121** 163201
[7] Shiner A D, Schmidt B E, Trallero-Herrero C, Wörner H J, Patchkovskii S, Corkum P B, Kieffer J C, Légaré F and Villeneuve D M 2001 *Nat. Phys.* **7** 464
[8] Wang G L, Jin C, Le A T and Lin C D 2012 *Phys. Rev. A* **86** 015401
[9] Wörner H J, Bertrand J B, Fabre B, Higuet J, Ruf H, Dubrouil A, Patchkovskii S, Spanner M, Mairesse Y, Blanchet V, Mevel E, Constant E, Corkum P B and Villeneuve D M 2011 *Science* **334** 208
[10] Itatani J, Levesque J, Zeidler D, Niikura H, Pepin H, Kieffer J, Corkum P B and Villeneuve D 2004 *Nature* **432** 867
[11] Baker S, Robinson J, Haworth C, Teng H, Smith R, Chirila C, Lein M, Tisch J and Marangos J 2006 *Science* **312** 424
[12] Smirnova O, Mairesse Y, Patchkovskii S, Dudovich N, Villeneuve D, Corkum P B and Ivanov M Y 2009 *Nature* **460** 972
[13] Vodungbo B, Sardinha A B, Gautier J, Lambert G, Lozano M, Sebban S, Meltchakov E and Delmotte 2011 *Europhys. Lett.* **94** 54003
[14] Corkum P B and Krausz F 2007 *Nat. Phys.* **3** 381
[15] Hentschel M, Kienberger R, Spielmann C, Reider G, Milosevic N, Brabec T, Corkum P B, Heinzmann U, Drescher M and Krausz F 2001 *Nature* **414** 509
[16] Krausz F and Ivanov M 2009 *Rev. Mod. Phys.* **81** 163
[17] Song H, Lü X Y, Zhu R B and Chen G 2019 *Acta Phys. Sin.* **68** 184201 (in Chinese)
[18] Xia C L and Miao X Y 2015 *Chin. Phys. Lett.* **32** 043202
[19] Lü X Y, Zhu R B, Song H, Su N and Chen G 2019 *Acta Phys. Sin.* **68** 214201 (in Chinese)
[20] Corkum P B 1993 *Phys. Rev. Lett.* **71** 1994
[21] Dou G, Yu Y, Guo M, Zhang Y M, Sun Z and Li Y X 2017 *Chin. Phys. Lett.* **34** 038502
[22] Huang J J, Su L, Pu S Z, Sun S A and Zhang L Y 2016 *Chin. Phys. Lett.* **33** 104204
[23] Kang B and Hwang S T 2016 *Chin. Phys. Lett.* **33** 057201
[24] Wang L K and Duan F L 2019 *Acta Phys. Sin.* **68** 193101
[25] Liao T J, Lin B H and Wang Y H 2019 *Acta Phys. Sin.* **68** 187901 (in Chinese)
[26] Wang T H, Li A and Han B 2019 *Acta Phys. Sin.* **68** 187102 (in Chinese)
[27] Xu F and Zhang L 2019 *Chin. Phys. B* **28** 117403
[28] Hu R X, Ma X L, An C H and Liu J 2019 *Chin. Phys. B* **28** 117802
[29] Ghimire S, DiChiara A D, Sistrunk E, Ndabashimiye G, Szafruga U B, Mohammad A, Agostini P, DiMauro L F and Reis D A 2012 *Phys. Rev. A* **85** 043836
[30] Vampa G, McDonald C R, Orlando G, Klug D D, Corkum P B and Brabec T 2014 *Phys. Rev. Lett.* **113** 073901
[31] Wu M, Browne D A, Schafer K J and Gaarde M B 2016 *Phys. Rev. A* **94** 063403
[32] Wu M, Ghimire S, Reis D A, Schafer K J and Gaarde M B 2015 *Phys. Rev. A* **94** 043839
[33] Ghimire S and Reis D A 2019 *Nature* **15** 10
[34] McDonald C R, Vampa G, Corkum P B and Brabec T 2015 *Phys. Rev. A* **92** 033845
[35] Vampa G, McDonald C R, Orlando G, Corkum P B and Brabec T 2015 *Phys. Rev. B* **91** 064302
[36] Tamaya T, Ishikawa A, Ogawa T and Tanaka K 2016 *Phys. Rev. Lett.* **116** 016601
[37] Ikemachi T, Shinohara Y, Sato T, Yumoto J, Kuwata-Gonokami M and Ishikawa K L 2017 *Phys. Rev. A* **95** 043416
[38] McDonald C R, Vampa G, Corkum P B and Brabec T 2017 *Phys. Rev. Lett.* **118** 173601
[39] Vampa G, Hammond T G, Thiré N, Schmidt B E, Légaré F, McDonald C R, Brabec T, Klug D D and Corkum P B 2015 *Phys. Rev. Lett.* **115** 193603
[40] Vampa G, McDonald C R, Orlando G, Klug D D, Corkum P B and Brabec T 2014 *Phys. Rev. Lett.* **113** 073901
[41] Guan Z, Zhou X X and Bian X B 2016 *Phys. Rev. A* **93** 033852
[42] Jin J Z, Xiao X R, Liang H, Wang M X, Chen S G, Gong Q and Peng L Y 2018 *Phys. Rev. A* **97** 043420
[43] Tancogne D N, Mücke O D, K?rtner F X and Rubio A 2017 *Phys. Rev. Lett.* **118** 087403
[44] Luu T T, Garg M, Kruchinin S Y, Moulet A, Hassan M T and Gouliel-makis E 2015 *Nature* **521** 498
[45] Ndabashimiye G, Ghimire S, Wu M, Browne D A, Schafer K J, Gaarde M B and Reis D A 2017 *Nat. Phys.* **13** 345
[46] Sivis M, Taucer M, Vampa G, Johnston K, Staudte A, Naumov A Y, Villeneuve D M, Ropers C and Corkum P B 2017 *Science* **357** 330
[47] Tancogne D N, Mücke O D, Kärtner F X and Rubio A 2017 *Nat. Commun.* **8** 745
[48] Taucer M, Hammond T J, Corkum P B, Vampa G, Couture C, Thiré N, Schmidt B E, Légaré F, Selvi H, Unsuree N, Hamilton B, Echtermeyer T J and Denecke M A 2017 *Phys. Rev. B* **96** 195420
[49] Yang J L, Yuan Q C, Chen R F, Fang H L, Xiao F J, Li J T, Jiang B Q, Zhao J L and Gan X T 2019 *Acta Phys. Sin.* **68** 214207 (in Chinese)
[50] Liu L, Zhao J, Yuan J M and Zhao Z X 2019 *Chin. Phys. B* **28** 114205
[51] Li L, Lan P F, Zhu X S, Huang T F, Zhang Q B, Lein M and Lu P X 2019 *Phys. Rev. Lett.* **122** 193901

[52] Zeng A W and Bian X B 2020 *Phys. Rev. Lett.* **124** 203901
[53] Wang X Q, Xu Y, Huang X H and Bian X B 2018 *Phys. Rev. A* **98** 023427
[54] Jiang S C, Chen J G, Wei H, Yu C, Lu R F and Lin C D 2018 *Phys. Rev. Lett.* **120** 253201
[55] Jiang S C, Wei H, Chen J G, Yu C, Lu R F and Lin C D 2017 *Phys. Rev. A* **96** 053850
[56] Li J B, Zhang X, Fu S L, Feng Y K, Hu B T and Du H C 2019 *Phys. Rev. A* **100** 043404
[57] Wang H Q, Feng Y K, Fu S L, Li J B, Zhang X and Du H C 2019 *Phys. Rev. A* **99** 023406
[58] Kelardeh H K, Apalkov V and Stockman M I 2015 *Phys. Rev. B* **91** 045439
[59] Liu C, Zheng Y, Zeng Z and Li R 2018 *Phys. Rev. A* **97** 063412
[60] Zurrón Ó, Picón A and Plaja L 2018 *New J. Phys.* **20** 053033
[61] Zurrón Ó, Boyero-García R, Hernández-García C, Picón A and Plaja L 2019 *Opt. Express* **27** 7776
[62] Ishikawa K L 2010 *Phys. Rev. B* **82** 201402
[63] Wallace P R 1947 *Phys. Rev.* **71** 622
[64] Slonczewski J C and Weiss P R 1958 *Phys. Rev.* **109** 272
[65] Saito R, Dresselhaus G and Dresselhaus M 1999 *Physical Properties of Carbon Nanotubes* (London: Imperial College Press) pp. 17–29
[66] Ishikawa K L 2013 *New J. Phys* **15** 055021
[67] Higuchi T, Heide C, Ullmann K, Weber H B and Hommelhoff P 2017 *Nature* **550** 224
[68] Dimitrovski D, Madsen L and Pedersen T 2017 *Phys. Rev. B* **95** 035405
[69] Naib I, Sipe J E and Dignam M M 2016 *Phys. Rev. B* **90** 245423
[70] Chizhova L A, Libisch F and Burgdörfe J 2016 *Phys. Rev. B* **94** 075412
[71] Yoshikawa N, Tamaya T and Tanaka K 2017 *Science* **356** 736
[72] Budil K S, Salières P, L'Huillier A, Ditmire T and Perry M D 2003 *Phys. Rev. A* **48** R3437
[73] Schubert O, Hohenleutner M, Langer F, Urbanek B, Lange C, Huttner U, Golde D, Meier T, Kira M, Koch S W and Huber R 2014 *Nat. Photon.* **8** 119
[74] Hasan M Z and Kane C L 2010 *Rev. Mod. Phys.* **82** 3045
[75] Chen L 2019 *Chin. Phys. B* **28** 117304